

Intermediate-velocity atomic collisions: Electron capture and loss in 10–42-MeV C ions

R. Anholt,* X.-Y. Xu,[†] Ch. Stoller,[‡] J. D. Molitoris,[§] and W. E. Meyerhof
Department of Physics, Stanford University, Stanford, California 94305

B. S. Rude and R. J. McDonald

Accelerator and Fusion Research Division, Lawrence Berkeley Laboratory, University of California, Berkeley California 94720

(Received 22 June 1987)

The capture and loss of electrons for incident bare, one-, two-, and three-electron 10–42-MeV carbon ions are studied. The one-electron-loss cross sections are compared with Glauber-approximation 1s ionization calculations, and a way of incorporating target-atom screening into the Glauber theory is proposed. The electron-capture cross sections agree reasonably well with eikonal-approximation results. The equilibrium charge states of the highest-energy C ions emerging from solid targets can be calculated accurately from gas-target equilibrium charge states using a theory incorporating excited-state effects.

I. INTRODUCTION

In recent years, this group has studied intermediate-energy collisions by measuring the capture and loss of mainly *K*-shell electrons in relativistic heavy-ion-atom collisions.^{1–5} Despite the enormous energies of the Xe and U ions used, the ion velocities (v) are approximately equal to those of the active *K*-shell electrons (v_K), thus the collision energies are intermediate between the low-velocity regimes where $v/v_K \ll 1$ and where molecular-orbital effects are important,⁶ and the high-velocity regimes ($v/v_K \gg 1$) where high-energy theories like the plane-wave Born approximation (PWBA) for ionization^{7–10} and the eikonal^{11–16} or other theories¹⁷ for capture are applicable. The challenge to atom-collision theory in this regime is to find adequate theories of electron capture and loss that bridge the two regimes. Since the high-energy approximations are usually simpler than the molecular theories, the approach we have taken is to formulate new or examine existing approximations that attempt to correct the high-velocity approximation.

For *K*-shell ionization we have examined the theories of Basbas and co-workers^{8–10} who introduce binding-energy and polarization corrections to the PWBA. Although these have been successful for target *K*-shell ionization by light projectiles at intermediate velocities, they appear not to work for projectile ionization.^{3,5} As is well known from studies of $p + H$ collisions,^{3,5,18,19} we have found that projectile ionization cross sections relative to PWBA predictions decrease with the perturbing target-atomic charge for Z_t greater than 0.2 times the projectile charge Z_p , whereas the theories of Basbas *et al.* predict they should increase due to the polarization effect. The Glauber approximation of McGuire and co-workers^{18,19} gives better agreement with experiment, except possibly at very low Z_t . Since the binding and polarization correction formulation is based on an expansion in Z_t/Z_p (for projectile ionization) it should perhaps not be too surprising to find it breaks down when Z_t/Z_p approaches or exceeds unity.

In comparing measured projectile ionization cross sections with theory it is important to take into account the

electron screening of the perturbing target nucleus.^{1,20–22} Although it is only possible to calculate this exactly for projectile *K*-shell ionization by hydrogen target atoms, an approximation has been formulated based on a separation of screening effects into contributions due to screening of the target charge and due to antiscreening (the excitation of projectile electrons by the target electrons). For relativistic projectile ionization by targets with $Z_t \geq 4$, antiscreening effects are never very large, and our approximate theories work reasonably well. Our formulation is less successful for excitation of low- Z ions by H_2 and He atoms, as will be shown in the present paper.

For electron capture, a large number of new high-velocity theories have been formulated in recent years such as the eikonal, strong-potential Born, impulse, and continuum distorted-wave Born approximations. The genealogical relationships between these approximations has been reviewed by Dubé.¹⁷ Our work has focused on the eikonal approximation.^{2,5} For heavy ions, a fully relativistic version of this approximation was formulated,¹¹ allowing calculations to be made of electron-capture transitions from any $n = 1, 2$, or 3 state of the target to any state of the projectile. For low- Z , nonrelativistic ions, a nonrelativistic formulation based on hydrogenic wave functions is available.^{14–16}

A subtheme in our work with relativistic heavy ions explored the role of excited-state effects in determining the equilibrium charge states of ions emerging from solid targets. Ions emerging from solid targets have higher charge states (fewer electrons) than ions emerging from gas targets.^{23–25} Electrons excited to or captured into excited states have a high probability of being ionized before they decay to the ground state in solid targets. We found that for zero-, one-, or two-electron ions, these effects can be calculated accurately using measured 1s ionization and total capture cross sections from thin-target experiments where excited-state effects play no role, and using calculated excitation, excited-state ionization, and excited-state capture cross sections relative to the measured cross sections. However, due to technical limitations, these theories could not be tested with gas

targets for relativistic heavy ions. We can test these theories using light ions, however.

In the present series of measurements, we used 0.8–3.5-MeV/amu C ions, available at the Stanford Van de Graaff accelerator, where v/v_K ranged from unity to about 2. There are three advantages of making measurements with these light ions. First, the perturbing Z dependence of the electron-capture and -loss cross sections can be studied over a much wider relative range of perturbing charge (Z_i/Z_p up to 9) than was available for relativistic heavy ions where Z_i/Z_p (<2) was bounded by the end of the Periodic Table. Second, we can study antiscreening effects in collisions with H (H_2) and He targets where the effect relative to the screening effect is largest. Finally, we can study excited-state effects on the equilibrium charge states in measurements where both gas-target and solid target data can be obtained.

Section II of this paper describes the apparatus set up to make gas- and solid-target measurements at the Stanford Van de Graaff accelerator. Section III gives results for electron loss (Sec. III A), electron capture (Sec. III B), and the equilibrium charge states of 42-MeV C ions (Sec. III C). Finally, Sec. IV contains the conclusions.

II. EXPERIMENT

Figure 1 shows the apparatus constructed to measure C-ion charge states at the Stanford FN tandem Van de Graaff accelerator. Carbon ions of selected charge states +3, +4, +5, and +6 were obtained at the analyzing magnet or by post-stripping between the analyzing magnet and switching magnet. In the latter case, the switching magnet selected the charge state. The beam enters a 6-cm-long differentially pumped gas cell, is analyzed by 80-cm-long deflection plates, and eventually arrives at a parallel-plate avalanche counter, which counts every particle. Attenuating screens or analyzing slits were used to keep the beam intensity at the counter below about 10^4 Hz.

The differentially pumped gas target consists of a cell with 4.88-mm² area entrance and exit apertures of 4.88 mm² area. The area around the cell is pumped by a 1000-l/sec diffusion pump. The beam travels only 6 cm through the outer chamber. Another set of 4.8-mm² entrance and exit apertures keeps the remaining beam line at high vacuum. The pressure of the gas cell was measured using a calibrated (relative to a McLeod gauge) mks capacitance manometer. For solid-target equilibrium charge-state measurements, the cell was removed, and was replaced with a wheel containing up to 15 targets.

The base vacuum of the beam lines and the chamber containing the gas cell is less than 10^{-6} torr. Due to the finite pumping speed of the diffusion pump and the up and downstream turbomolecular pumps, the pressure of both the gas-cell chamber and the surrounding beam lines increases with the gas-cell pressure. Since the projectile can also be stripped in the surrounding beam line or chamber, but the gas is essentially the same as in the gas cell (for surrounding pressures exceeding the base vacuum), this just increases the effective pressure in the

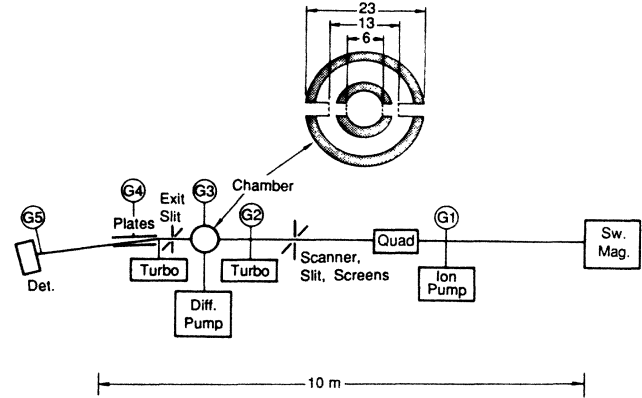


FIG. 1. Schematic diagram showing the layout of the experimental apparatus (to scale). Gauges G1, G2, G3, G4, and G5 are cold-cathode gauges. The 6-cm-diam inner-cell pressure is measured with a capacitance manometer. Quad, quadrupole magnet; Turbo, turbomolecular pump (260 l/sec); Diff. Pump, diffusion pump (1000 l/sec); Sw. Mag., switching magnet. The inner chamber dimensions are in centimeters.

cell, which we have estimated to be less than 1%.

The deflection plates and the length of tube downstream of the plates were chosen to give a charge-state dispersion of 1 cm per charge state for 60-MeV oxygen ions with a voltage <40 kV/cm. For 10–42-MeV C ions, less than 10 kV was applied to the plates.

The detector used is a position-sensitive, delay-line-type parallel-plate avalanche counter (PPAC). The advantage of a PPAC is that it can sustain high count rates without undergoing radiation damage,²⁶ and it is very fast. The disadvantage is that the signal pulses are very small and highly dependent on the high voltage applied. Also, an electronically stabilized gas system must be used to keep the counter pressure stable at less than 10 torr, since pressure drifts of less than ± 1 torr usually set off detector sparking.

Figure 2 illustrates the principle of the PPAC detector, and a typical charge-state spectrum. The anode of this detector consists of 50 pads etched onto a printed circuit board, each of which are connected to a delay line consisting of a series of passive integrated-circuit chips.²⁷ The time difference between the signal arriving at opposite ends of the delay line is measured using constant fraction timing discriminators and a time to amplitude convertor. The detector has a double window of 150- $\mu\text{g}/\text{cm}^2$ stretched aluminized Mylar. The outer window bows with the differential gas pressure; the inner window stays parallel to the printed circuit board plane. The window to anode spacing is approximately 3 mm. Approximately 600 V (just below the point where the detector is prone to spark) is applied to the inner and outer windows on the anode side. LeCroy 612A scintillation amplifiers are used to obtain a gain of 100. With 10-MeV C ions, the signal after amplification is 150–300 mV in amplitude, has a rise time of less than 7 nsec (oscilloscope limited), returns to the baseline in 30 nsec, and is well separated from the noise. Due to the attenuation in the delay line, a different signal amplitude is obtained, depending on which side of the detector the

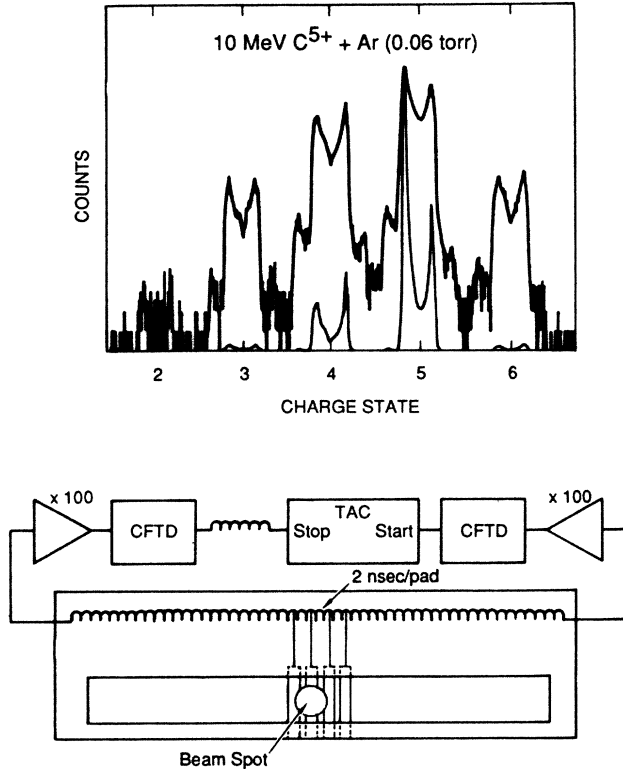


FIG. 2. Schematic diagram showing part of the parallel-plate avalanche detector, associated electronics, and a typical charge-state spectrum (drawn on linear and logarithmic scales using thin and thick lines). For each charge state, multiple peaks are seen because the beam could hit one of three to four pads. The distance between pads is 2 mm, and the corresponding time difference in the spectrum is 4 nsec. (TAC, time-to-amplitude converter; CFTD, constant-fraction timing discriminator.)

beam strikes. We have also noted local amplitude variations.²⁶ If the discriminators are set too high, some charge-state fractions can be miscounted as a result of these variations. Hence, a series of careful measurements of relative charge states was done before every run to assure that the relative efficiency of the detector is flat over the active region.

For each target, the relative charge-state yields were measured at four to five target pressures. For low target thicknesses, the equations for determining the fraction of projectiles entering with charge-state i and exiting in the j th charge state can be approximated as

$$Y_{j,i} - B_{j,i} = c \sigma_{i,j} PL + O(P^2) + \dots,$$

also we define

$$Y_{i,i} - B_{i,i} = -c \sum_{j \neq i} \sigma_{i,j} PL + O(P^2) + \dots, \quad (1)$$

where c is a constant, P is the target pressure in torr, L is the target cell length, and $B_{j,i}$ is the background yield due to electron capture and loss in the residual beam-line vacuum or incomplete charge-state selection by the switching magnet. The background yields were measured at zero target pressure approximately 4–5 times

for every beam energy and incident charge state. They were found to be smaller than 0.5% for $j \neq i$ ($B_{i,i} \geq 0.995$), and did not change much from measurement to measurement. For very large pressures, terms with higher order than P^2 are important, therefore we kept $Y_{i,i} > 0.8$ in the measurements. For each pressure $Y_{i,j} - B_{i,j}$ was divided by cPL to obtain a cross section, which was then least-squares fitted to a straight line to extrapolate σ_{ij} at $P=0$. Terms of order P^2 and higher are thereby eliminated. For the incident charge state, we fit $(Y_{i,i} - B_{i,i})/cPL$ to a straight line to obtain $\sum \sigma_{ij}$, which generally was found to be equal to sum of all separately fitted σ_{ij} values within about 10%.

The statistical experimental uncertainties were generally smaller than $\pm 1\%$. The largest error comes from the measurements of target pressure which has at least a ± 1 mtorr uncertainty. Since the smallest pressures were used with the heaviest targets, the largest absolute experimental errors were obtained there.

Finally, we should mention that for measuring the equilibrium charge states of the thick-solid targets and the heavy Kr and Xe gas targets, we had to collimate the exiting beam with the exit slits shown in Fig. 1. In these cases, the multiple scattering cone gave a 1–3-cm-diam beam spot at the detector without exit slits, making the separation of charge states impossible. We note that in any charge-state measurement, certain large scattering angles are cut off by the exit collimator; the use of a downstream collimator in the present measurement reduced the largest scattering angle more than usual. We verified that the same relative charge-state fractions were obtained when the slits were opened by a factor of 2 wider than nominal.

III. RESULTS AND DISCUSSION

A. Electron ionization cross sections

Figure 3 compares measured C^{5+} ionization cross sections in gas targets with Glauber-approximation calculations.^{18–19} The unscreened Glauber cross sections agree reasonably well with measurements even for very large ratios of the perturbing charge Z_t to the projectile charge; $Z_t/Z_p = 9$ for the heaviest target. The Glauber approximation agrees reasonably well with measurements of projectile ionization using relativistic heavy ions also, though the highest ratio Z_t/Z_p tested there was only about 2. Our cross sections agree with cross sections for $C^{5+} + He$ collisions measured by Dillingham *et al.*²⁸

In comparing measured and calculated ionization cross sections, it is important to realize that the perturbing charge Z_t is partially screened by the target electrons. In our work using relativistic heavy ions,^{1–3} we took this screening into effect by replacing the target factor Z_t^2 by

$$S(q) = \left| Z_t - \sum_i \langle \psi_i | \exp(i\mathbf{q} \cdot \mathbf{r}) | \psi_i \rangle \right|^2 + Z_t - \sum_i | \langle \psi_i | \exp(i\mathbf{q} \cdot \mathbf{r}) | \psi_i \rangle |^2, \quad (2)$$

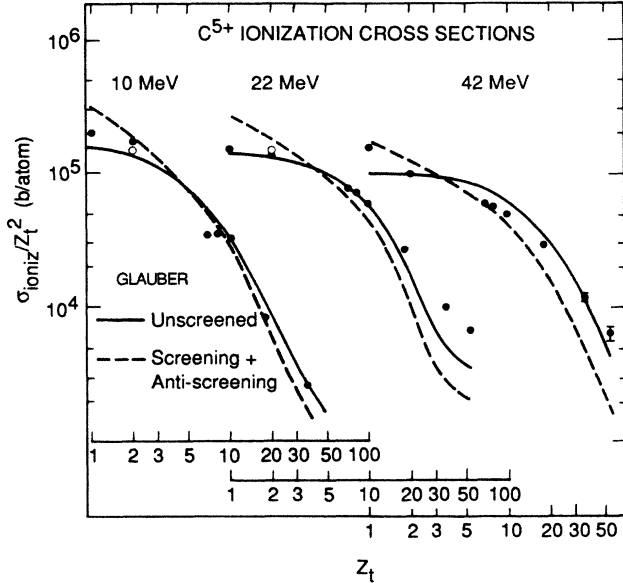


FIG. 3. Measured C^{5+} single-ionization cross sections (closed circles) compared with Glauber-approximation calculations. Most experimental uncertainties are smaller than the data points. The solid lines were calculated omitting target screening, and the dashed lines including screening and anti-screening. The open circles are from Ref. 28.

where ψ_i is the target atomic orbital for the i th electron, and the sum includes all target electrons. In this expression, q is the momentum transferred from the incident target system (in the projectile frame) to the projectile $1s$ electron. $S(q)$ is incorporated into the integral over momentum transfer. In the Glauber approximation the ionization cross section is given by¹⁸⁻¹⁹

$$\sigma_{\text{loss}} = \sum_{l,m} \int dk \int dq S(q) |G(k, \mathbf{q}, lm, ls)|^2, \quad (3)$$

where k is the momentum and l, m are the quantum numbers describing the final state of the ionized electron, and G is the Glauber ionization amplitude obtained by Golden and McGuire.¹⁸ The insertion of the screen-

ing factors into Eq. (3) was suggested in Glauber calculations by Franco²⁰ (who did not include antiscreening factors, however).

The first term in Eq. (2) is the effective screened target charge; as q approaches zero at high projectile velocities, the charge vanishes. Then, ionization, which would normally occur at large impact parameters does not occur because the projectile sees a fully screened target nucleus. For low velocities, where excitation occurs at small impact parameters, and where the projectile sees a nearly bare target nucleus, q is large so the sum of matrix elements of $\exp(i\mathbf{q}\cdot\mathbf{r})$ is much smaller than Z_t . The antiscreening term, given by the middle term in Z_t in Eq. (2), is the contribution to projectile ionization by the Z_t separate target electrons. If q is large, the ionization cross section varies as $Z_t^2 + Z_t$, where Z_t^2 comes from the Coulomb potential between the target nucleus and electron, and the factor Z_t comes from Z_t separate electron-electron interactions. At $q \rightarrow 0$, ionization by the fully screened neutral target atom cannot occur; therefore the last term is a correction factor which cancels the Z_t factor at $q = 0$. We obtained the matrix elements from tabulated Compton scattering form factors,²⁹ which are based on Hartree-Fock atomic wave functions. The approximation needed to obtain the sum of the squares of matrix elements in the last term of Eq. (2) is discussed in paper II.¹

The present data does not consistently support the application of these screening factors to the Glauber approximation. At low Z_t , the data are in better agreement with the unscreened calculations (see discussion below). At high Z_t in 22- and 42-MeV C^{5+} collisions, the data are also in better agreement with the unscreened Glauber-approximation results, but at high Z_t in 10-MeV C^{5+} collisions, the data agrees better with the screened Glauber. The calculated screening effect is never very large, though it reduces the cross sections by a factor of ~ 0.5 at the highest Z_t , and, due to antiscreening, increases them by a factor of 2 at $Z_t = 1$ [where $(Z_t^2 + Z_t)/Z_t = 2$].

For collisions with H atoms the screening and antiscreening effects can be calculated exactly in the PWBA using²²

$$\sigma_{\text{loss}} \sim \sum_{l,m} \int_0^\infty dk \sum_{n',l'} \int_{q_0}^\infty \frac{dq}{q^3} |\langle klm | \exp(i\mathbf{q}\cdot\mathbf{r}) | 1s \rangle|^2 |\langle n'l' | Z_t - \exp(i\mathbf{q}\cdot\mathbf{r}) | 1s \rangle|^2, \quad (4)$$

where $n'l'$ are final states of the target atom, the sum including the continuum states, and q_0 is given by

$$q_0 = \frac{E_{1s}(Z_p) + \frac{1}{2}k^2 + E_{1s}(Z_t) - E_{n'l'}(Z_t)}{v}. \quad (5)$$

Equation (2) is an approximation to Eq. (4); valid when the momentum lost in exciting a target electron to the state $n'l'$ is negligible compared to the momentum need-

ed to excite the projectile electron. This approximation clearly works best if the momenta are small (high velocity) or if the target electron is lightly bound [$E_{1s}(Z_t) \ll E_{1s}(Z_p)$].

Equation (4) can be evaluated exactly for collisions with H atoms. Unfortunately we have not measured C^{5+} ionization by H atoms, but with H_2 molecules and with He atoms. In comparing Eq. (4) with measurements, we assume that the H_2 molecule is equivalent to two H atoms, hence we divide the cross section per mol-

ecule by 2. Screening is important only at high q , where the H momentum wave functions are not disturbed much by molecular interactions. One neglects possible molecular vibrational and rotational excitations in summing over $n'l'$, however. For He, we assume an effective target charge of 1.7.²¹ Figure 4 compares measured H₂- and He-induced C⁵⁺ ionization cross sections with PWBA calculations (assuming unscreened target charges) and with Eq. (4). With the possible exception of the 42-MeV H₂ point, the data agree better with the unscreened PWBA calculations. One possible reason for this is that we have to assume that binding effects are negligible in the comparisons, thus one would expect the cross sections to fall below both curves. The better agreement with the PWBA may therefore be a fortuitous result of neglecting binding effects.

Another theory that has been used to calculate projectile ionization cross sections is the unitarized semiclassical approximation (SCA) of Kaneko.³⁰ He calculates the excitation (P_{exc}) and ionization (P_{ioniz}) probabilities at each impact parameter b . In general for $Z_t > Z_p$, these probabilities tend to exceed unity. To preserve unitarity he calculates the unitarized ionization probability using

$$P_{\text{unit ioniz}} = \frac{P_{\text{ioniz}}}{P_{\text{tot}}} \sin^2 \sqrt{P_{\text{tot}}}, \quad (6)$$

where $P_{\text{tot}} = P_{\text{exc}} + P_{\text{ioniz}}$. In addition, he takes target screening (but not antiscreeing) into account by using a Moliere potential.³⁰ As shown in Fig. 5, his calculations of 10-MeV C⁵⁺ ionization by N₂, O₂, Ne, and Ar atoms come reasonably close to fitting our measured cross sections.

The good agreement is not due to the unitarization,

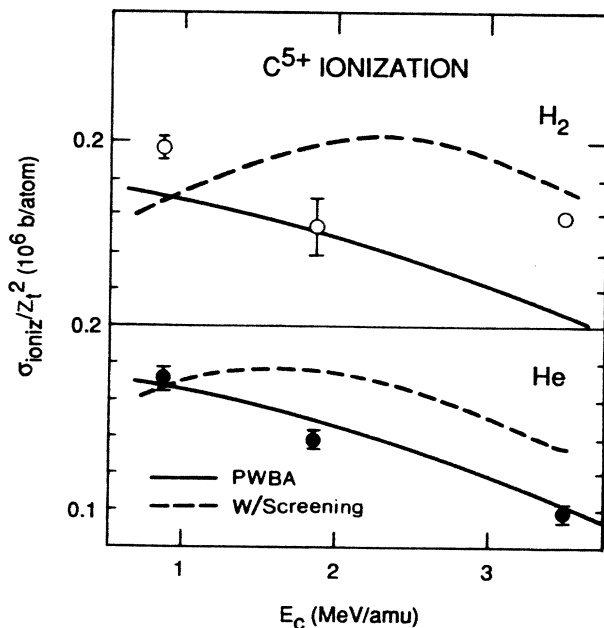


FIG. 4. Measured C⁵⁺ single-ionization cross sections in H₂ and He targets compared with unscreened PWBA calculations (solid lines) and calculations with screening using Eq. (4) (dashed lines).

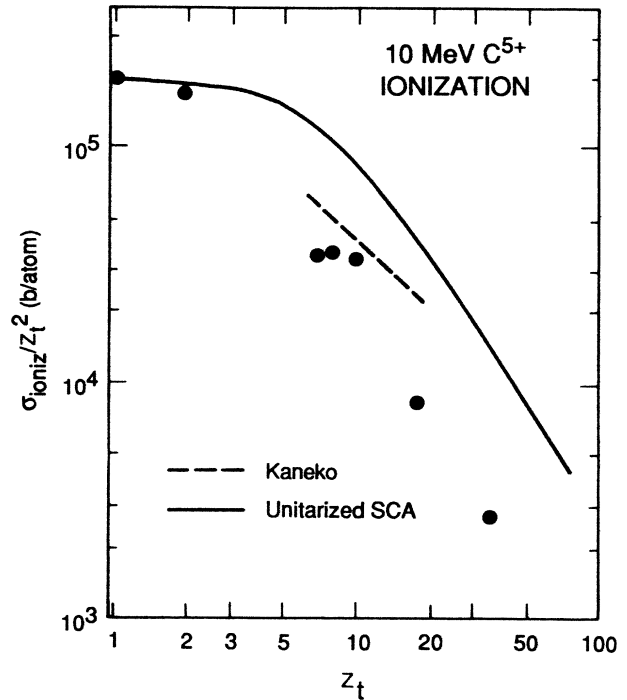


FIG. 5. Measured 10-MeV C⁵⁺ ionization cross sections compared with calculations of Kaneko (Ref. 30) (dashed line) and unitarized SCA calculations (solid line).

but to another approximation Kaneko uses: the use of a plane wave to describe the final state of the ionized electron. It is well known that Coulomb waves must be used to describe the states of the low-energy ionized electrons.⁷ We recalculated the 10-MeV C⁵⁺ ionization cross sections using Kaneko's method, but using the semiclassical ionization probabilities of Hansteen *et al.*³¹ with Coulomb electron waves. We assume that $P_{\text{exc}} \approx P_{\text{ioniz}}$, which is found to hold for the total PWBA cross sections. For $Z_t > 3$, we took into account target screening by using an effective target charge $Z_{\text{eff}} < Z_t$, obtained by comparing Glauber calculations with screening to those without screening. The calculated cross sections were normalized to experiment at $Z_t = 1$. As shown in Fig. 5, the properly calculated, unitarized SCA cross sections exceed the measured cross sections significantly. From this we conclude that unitarity effects are not the primary effects responsible for the falloff of the reduced ionization cross sections σ/Z_t^2 with increasing Z_t . We interpret the falloff as a binding effect. It is possible that both binding and unitarity effects are present; however, if the binding effect is sufficiently strong to keep the ionization probabilities from ever approaching unity, unitarity effects may never come into play. These questions are best investigated with coupled-channel calculations.³²

B. Electron-capture cross sections

Figure 6 compares measured single-electron-capture cross sections with nonrelativistic eikonal-approximation calculations.¹⁴⁻¹⁶ In these eikonal calculations, hydro-

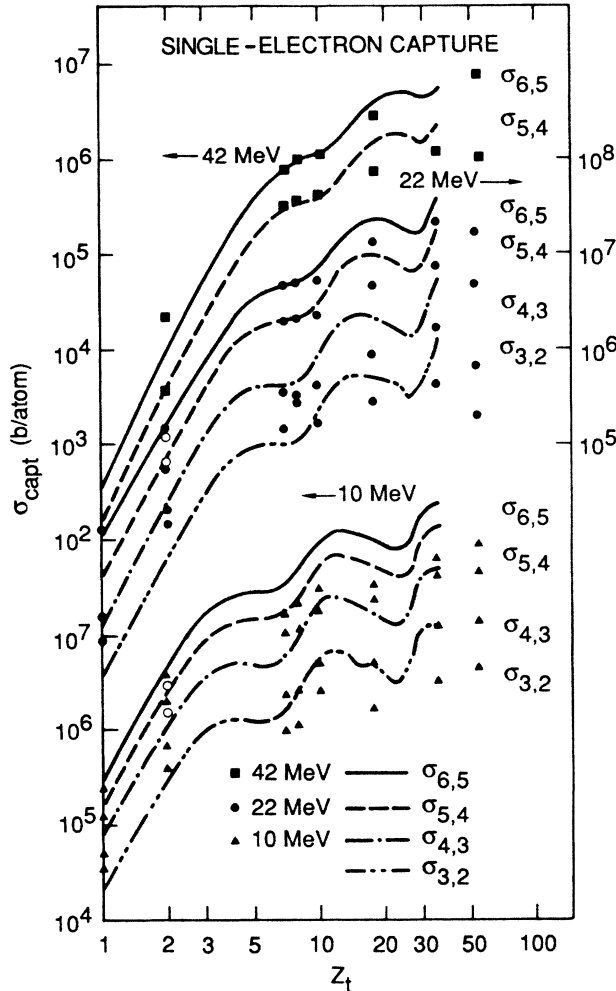


FIG. 6. Measured electron-capture cross sections compared with eikonal-approximation calculations. The closed squares, circles, and triangles are measured for 42-, 22-, and 10-MeV C-ions and the solid, dashed, dash-dotted, and dash-dot-dotted curves are absolute eikonal calculations for C^{6+} , C^{5+} , C^{4+} , and C^{3+} single-electron capture. The open circles were measured by Dillingham *et al.* (Ref. 28).

genic electron wave functions for the projectile and target shells were used. All projectile orbitals up to $n = 10$ were included, and all filled target shells were included. For the target wave functions, we used different Slater screening factors³³ ΔZ_t for each shell; however, we did not attempt to use effective noninteger quantum numbers, which are recommended for $n > 4$. We assumed that the target electron binding energies are given by $E_{nl} = \frac{1}{2}[Z_t - \Delta Z_t(n)]^2$, neglecting possible screening factors θ_n , found in ionization calculations.⁷ A satisfactory method of incorporating such factors in the eikonal approximation for electron capture has not been formulated to date.¹² For molecular targets, we assumed that atomic wave functions with the same Slater screening factors of the separated atoms can be used. Since high momentum transfers are involved, where the inner parts of the atomic wave functions matter the most, we believe that the neglect of target molecular effects is not a prob-

lem. For capture into partially filled shells (e.g., C^{4+}), we take into account the Pauli blocking of transitions into filled shells of the projectile, and use an effective projectile charge equal to the charge state (e.g., $Z_p = 4$ for C^{4+}). This approximation works best if most transitions are to outer shells of the projectile that see a full screened projectile charge.¹³ Finally, we used the prior form of the eikonal approximation in all cases. In our eikonal calculations for relativistic heavy ions, we formulated a higher- Z/n criterion for choosing the post or prior form depending on whether the ratio of the effective charge to the principal quantum of the projectile or target shell is largest. The relativistic electron-capture data did not consistently support this criterion. Since the application of this criterion makes the calculations much more complicated, and does not appear to improve the agreement much, we did not use this criterion. (Some sums over projectile shells can be done analytically in the prior form, but not if the higher- Z/n criterion is used.)

The measured cross sections generally agree within about a factor of 3 with the eikonal approximation. As the projectile velocity decreases, the differences between the data and the eikonal approximation become larger. The measured and calculated cross sections oscillate as a function of Z_t . This was also noted by Bell and Betz³⁴

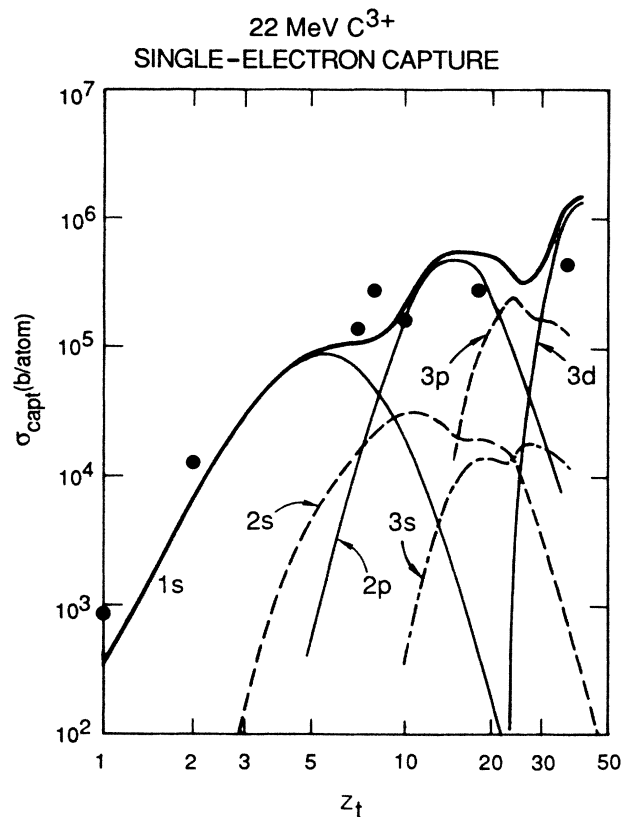


FIG. 7. Measured 22-MeV C^{3+} single-electron-capture cross sections compared with eikonal-approximation calculations. The thick solid line shows the total capture cross section. The thin solid lines show the capture cross sections from target orbitals with $n-l=1$, the dashed lines are for target orbitals with $n-l=2$, and the dash-dotted lines are for $n-l=3$.

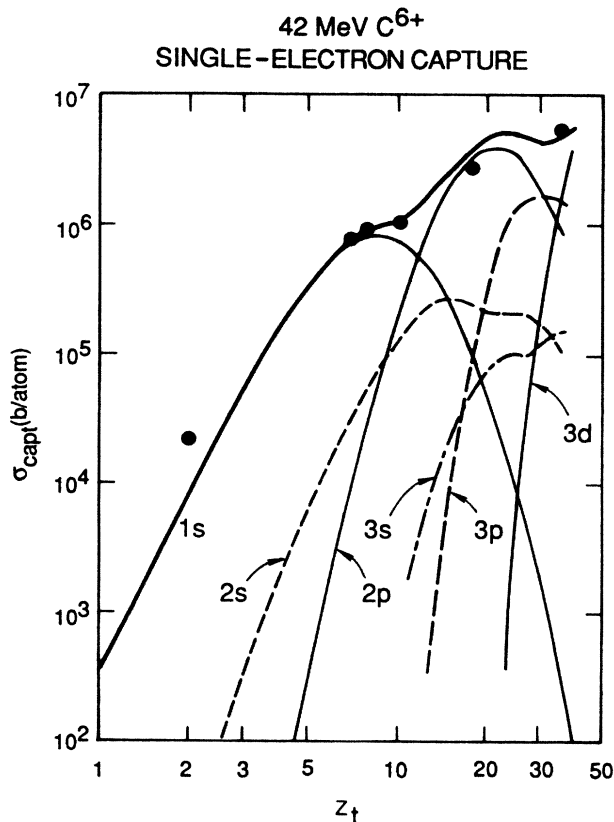


FIG. 8. Same as Fig. 7 for 42-MeV C^{6+} capture.

who used the Oppenheimer-Brinkman-Kramers³⁵ approximation for electron capture. The origin of these oscillations is illustrated in Figs. 7 and 8 where the individual contributions due to capture from various target shells are shown. From these figures we see that capture from target shells with $n-l=1$ is always dominant. With increasing $n-l$ the maximum capture cross sections decrease. The peak in each capture cross section occurs when the velocity of the captured target electron is equal to the velocity of the projectile K -shell electron: for target $1s$ electrons, the peak in the capture cross sections occurs at $Z_t \approx 6$, for $2p$ electrons, the peak occurs at $Z_t \approx 15[(Z_t - \Delta Z_t)/2 \approx 5.5]$, for $3d$ electrons it occurs at $Z_t \approx 36[(Z_t - \Delta Z_t)/3 \approx 5]$, and so on. It is interesting to note that in the low-velocity molecular regimes, peaks are seen in the total projectile vacancy production cross sections due to vacancy sharing of electrons promoted from orbitals with $n-l=1$.⁶

We believe that the primary improvements needed to bring the eikonal-approximation calculations into better agreement with measurements is to use more accurate electronic wave functions than Slater screened hydrogenic wave functions. The calculated cross sections are very sensitive to the parameters chosen to calculate the effective charge. Also, the Slater screened orbitals for high n and l are poor representations of many-electron wave functions, which can be seen by comparing Compton profiles at the momentum values q relevant to electron capture.³⁶

C. Equilibrium charge states

The equilibrium charge states of 22- and 42-MeV C ions emerging from gas and solid targets were obtained in three ways. In gas targets all 16 cross sections at 22 MeV (four cross sections at 42 MeV), σ_{ij} , for the transitions from ions with initial charge state equal to $i=3, 4, 5,$ and 6 (5 and 6 only for 42 MeV) to all other charge states j were measured. By setting the rate of change of each charge state equal to zero,

$$\frac{dY_{i,j}}{dT} = 0 = \sum_j \sigma_{ij} f_j, \quad i=3,4,5,6, \quad (7)$$

one can solve the coupled linear equations for the equilibrium charge-state fraction f_j . Second, for all gas targets except H_2 and He , one can measure the equilibrium charge state by using gas pressures in the cell less than about 2 torr (1 torr for Kr and Xe targets). The relative gas-target equilibrium charge-state fractions obtained using the first two methods agree within 20% for 22 MeV (10% for 42 MeV), as shown in Fig. 9. Finally, we measured the equilibrium charge states of solid targets using ~ 100 – 500 - $\mu g/cm^2$ metal foil targets. We corrected the equilibrium charge states for energy loss in the targets by plotting $f_j(E)$ versus ion energy, estimating df_j/dE , from which the correction Δf_j is obtained by multiplying by the energy loss ΔE in the target ($\Delta E = t dE/dx$, where dE/dx is the ion stopping power³⁷ and t is the target thickness). These corrections are smaller than 2%. For C targets, the charge-state fractions obtained using 5- and 120- $\mu g/cm^2$ targets agreed with 2%.

Figure 9 compares equilibrium charges states measured in gas and solid targets. The charge-state fractions

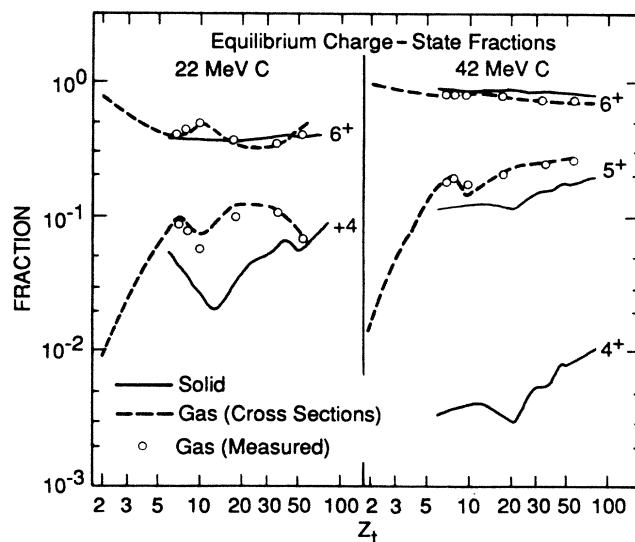


FIG. 9. Measured equilibrium charge-state fractions in 22- and 42-MeV C collisions. The 5+ fractions, which are approximately equal to the 6+ fractions, have been omitted at 22 MeV for clarity (the sum of the fractions is equal to unity). The solid and dashed lines connect points measured using solid and gas targets. The open circles give gas target equilibrium fractions calculated from measured thin-target cross sections.

oscillate with Z_t , in part due to the oscillating capture cross sections. We draw lines to guide the eye between the sparse data points in Fig. 9, but due to the complicated way the capture cross sections vary with Z_t , we cannot estimate how accurate these interpolations are. In general, we find higher charge states in solid targets; one clearly sees higher 6+ yields in solids at 22 MeV, and lower 5+ yields at 42 MeV. At low Z_t , the capture cross sections fall off faster with decreasing Z_t than the ionization ones, so that the charge-state fractions of the 6+ ions increase and the 5+ and 4+ rapidly decrease.

Some of the theories developed to explain the charge states of relativistic heavy ions in matter can be used to calculate the present gas-solid charge-state differences. For example, in paper II (Ref. 1) a formula for the equilibrium ratio R_{eq} of ions carrying an electron to bare ions was developed, which can be applied to calculating charge-state fractions at 42 MeV (where the fractions of two- and more-electron C ions is negligible). In gas and solid targets one obtains

$$R_{eq} = f_{5+} / f_{6+} = a_{tot} / s_1 \text{ for gases} \quad (8a)$$

$$= \frac{a_1}{s_1 + x_1 + x_2} \left[1 + \frac{x_1 + x_2}{s_2} \right] + \frac{a_2 + a_3}{s_2} \text{ for solids,} \quad (8b)$$

where $a_{tot} = a_1 + a_2 + a_3$ is the total capture cross section, a_1 is the capture cross section into the ground state, and $a_2 + a_3$ is that into excited states. Formula (8) is based on a four-state model that includes only $1s$, $2s$, and $2p$ projectile states, but we interpret $a_2 + a_3$ as the total capture cross section into all excited states. Similarly $x_1 + x_2$ is the excitation cross section from the $1s$ to the $2s$ and $2p$ states, which we interpret as the total excitation cross section from the $1s$ state to all bound states. Finally, s_1 and s_2 are $n=1$ and $n=2$ ionization cross sections.

Equation (8a) for gases has a simple interpretation. For gases, the time between collisions is long so that ions excited to or captured into high bound states always decay to the ground state; the equilibrium fraction is therefore the total capture cross section divided by the ground-state ionization cross section. In solids, electrons captured into excited states (cross section $a_2 + a_3$) usually are ionized (with larger cross sections s_2) before they decay, hence for the part of R_{eq} due to excited-state capture, one divides by the higher $n=2$ ionization cross section. This gives an upper bound on R_{eq} , since electrons captured into $n=3$ and higher states have an even larger ionization cross section. If electrons are captured into the ground state, they can either be ionized or excited to high bound states. Once excited, they can be ionized with cross section s_2 . The quantity $(s_1 + x_1 + x_2) / [1 + (x_1 + x_2) / s_2] / s_1$ is the increase in the effective $1s$ ionization cross section due to excitation. One obtains less than the full increase $(s_1 + x_1 + x_2) / s_1$ since some electrons can be deexcited back to the ground state before ionization.

One can write the solid-target value of R_{eq} in terms of the gas-target value and ratios of cross sections as

$$R_{solid} = R_{gas} \left[\frac{s_1 [1 + (x_1 + x_2) / s_2]}{s_1 + x_1 + x_2} \frac{a_1}{a_{tot}} + \left[1 - \frac{a_1}{a_{tot}} \right] \frac{s_1}{s_2} \right]. \quad (9)$$

We can calculate the ratios of cross sections using the PWBA for excitation and ionization cross sections^{1,7} and the eikonal approximation¹⁴⁻¹⁶ for capture cross sections (see paper II for a description of the cross-section calculations). For instance, for 42-MeV C ions with $Z_t = 29$, we find $1 + (x_1 + x_2) / s_2 = 1.18$, $(s_1 + x_1 + x_2) / s_1 = 1.44$, $a_1 / a_{tot} = 0.57$, and $s_1 / s_2 = 0.39$, which gives $R_{solid} / R_{gas} = 0.63$. One obtains a lower value of R_{eq} for solid than gas targets; fewer C ions emerge from solids carrying electrons and the solid-target states are higher.

Figure 10 shows equilibrium ratios for 42-MeV C ions together with the reduction factor R_{solid} / R_{gas} . As Z_t increases from 4 to 100, the ratio varies slowly from 0.45 to 0.65. By multiplying the measured gas-target equilibrium ratios by this reduction factor, we obtain fairly good agreement with the measured solid-target equilibrium charge-state fractions.

The reduction of the solid-target equilibrium ratio comes approximately equally from both the loss of electrons captured into excited states and from the loss of excited electrons. About one-half of the total capture cross section into bare C^{6+} ions is into excited states. However, since s_2 is not infinite, not all of these excited electrons are lost, and some still contribute to R_{eq} . The

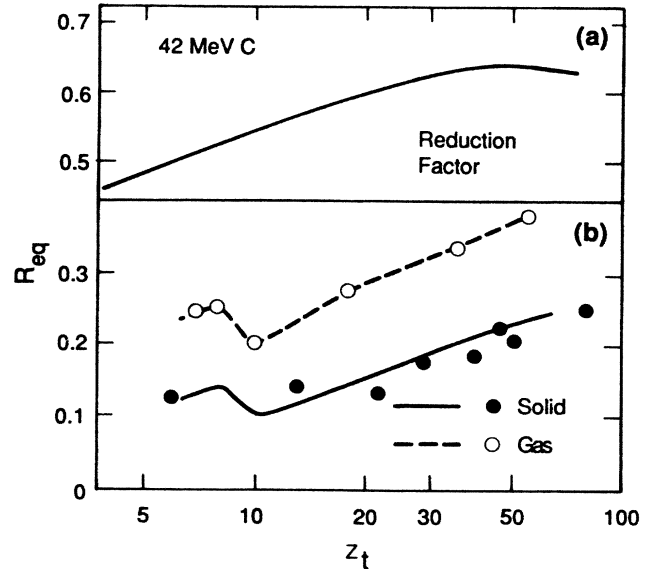


FIG. 10. (a) The reduction factor calculated from Eq. (9). (b) The ratio of emerging 42-MeV C ions carrying one electron to bare C ions measured in gas (open circles, dashed line to guide the eye) and solid (solid circles) targets. The solid line was calculated by multiplying the dashed line by the reduction factor at every Z_t .

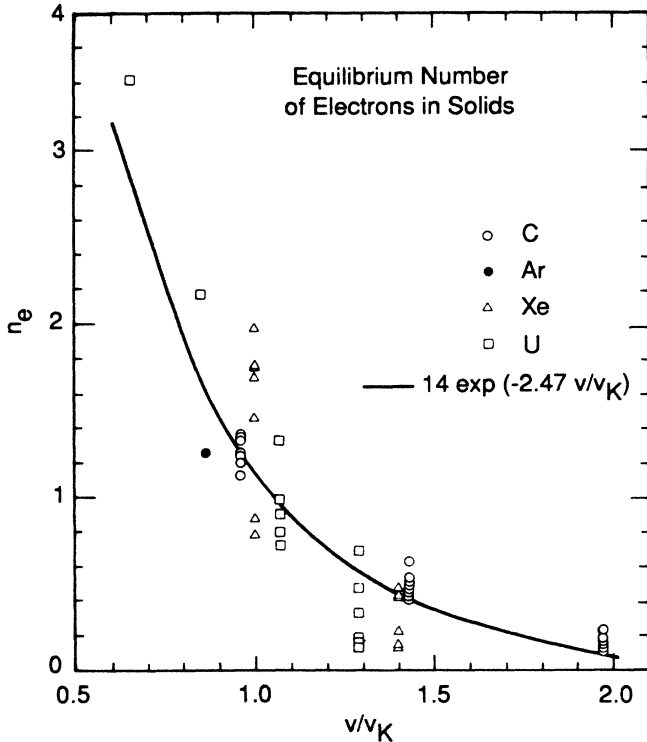


FIG. 11. The equilibrium number of projectile electrons plotted against v/v_K , where v_K is the K -electron velocity. The C, Xe, and U values are from the present work and papers V and VIII. The Ar data are from Ref. 40.

remaining reduction of the electrons captured to the ground state occurs due to excitation into $n=2$ and higher states. Therefore, neither the loss of excited electrons nor the loss of electrons captured into excited states is the dominant mechanism for producing higher solid-target charge states in 42-MeV C-ion collisions.

D. Equilibrium electron numbers

Most semiempirical formulas for the equilibrium charge states of ions in matter are based on the ideas of Bohr,³⁸ or Lamb,³⁹ who hypothesized that electrons with velocities less than the ion velocity or binding energies less than $\frac{1}{2}mv^2$, where m is the electron mass, will be stripped. Since in the Thomas-Fermi model, the electron velocities scale as $Z_p^{2/3}$, most formulas for the equilibrium charge states depend exponentially on a factor $\alpha v/v_0 Z_p^n$, where α is a numerical constant, v_0 is the atomic unit of velocity, and $n \approx \frac{2}{3}$.

For the stripping of the last projectile electron, the equal-velocity or equal-energy criterion both will predict that the charge state should depend on the ratio v/v_K , where v is the ion velocity (βc for relativistic ions) and $v_K (=Zv_0)$ is the projectile K -electron velocity. To investigate this scaling we plot the equilibrium number of electrons in solid targets versus v/v_K in Fig. 11. The average number of electrons is obtained from the equilibrium charge-state fractions using for C ions

$$n_e = f_{5+} + 2f_{4+} + 3f_{3+} + \dots, \quad (10)$$

with similar formulas for other ions. As we have seen in the present paper and in papers V and VIII,^{4,5} the equilibrium charge-state fractions depend on the target atomic numbers for several reasons: the interplay between ionization and radiative and nonradiative capture for relativistic ions, or oscillatory nonradiative capture cross sections for low- Z ions. Nevertheless, it is clear that for ions spanning the Periodic Table one indeed sees that n_e scales roughly with v/v_K . We fit the present electron numbers to

$$n_e = 14 \exp(-2.4v/v_K), \quad (11)$$

which is shown by the solid line in Fig. 11. The applicability of Eq. (11) is limited to $v/v_K > 0.8$. It is interesting to note that n_e is unity at $v/v_K = 1.05$ which is suggested by the criteria of Bohr and Lamb: for $v/v_K < 1$, the K electrons are more likely to be present ($n_e > 1$) and for $v/v_K > 1$, the K electrons are more likely to be absent ($n_e < 1$).

IV. CONCLUSIONS

The present measurements of charge-state fractions of intermediate-energy C ions in matter confirm the applicability of theories that have been explored in our relativistic heavy-ion studies of ionization, capture, and ion charge states¹⁻⁵ to nonrelativistic ions. In particular, we find good agreement between measured single-electron ionization and capture cross sections, and Glauber and eikonal-approximation calculations. For ionization, the Glauber approximation predicts ionization reasonably accurately, even when the ratio of the perturbing charge to the initial charge approaches 9. It is not clear whether electron screening and antiscreeing are being calculated properly in the present approximations. The better agreement found with the unscreened PWBA may be due to the neglect of binding effects or the use of approximate hydrogenic wave functions in the collisions with H_2 and He atoms. From the practical point of view of rapidly estimating ionization cross sections, the present data indicate that the neglect of screening effects is valid. To improve the agreement between measured capture cross sections and the eikonal approximation, emphasis should be placed on incorporating many-electron Hartree-Fock wave functions into the eikonal or other capture theories.

Finally, we have shown that formulas developed for relativistic ions to calculate the equilibrium ratio of ions carrying an electron to bare ions can be applied to 42-MeV C-ion collisions in gas and solid targets.

ACKNOWLEDGMENTS

This work was supported in part by the National Science Foundation, Grant Nos. PHY-83-13676 and PHY-86-14659 (Stanford) and by the U.S. Dept. of Energy, Contract No. DE-AC03-76SF00098 (Lawrence Berkeley Laboratory).

- *Present address: 1604 East River Terrace, Minneapolis, MN 55414.
- †Permanent address: Tsing Hua University, Beijing, People's Republic of China.
- ‡Present address: Nuclear Physics Department, Schlumberger Well Services, Houston, TX.
- §Present address: Department of Physics, Lawrence Livermore Laboratory, Livermore, CA.
- ¹R. Anholt, *Phys. Rev. A* **31**, 3575 (1985) (paper II).
- ²W. E. Meyerhof, R. Anholt, J. Eichler, H. Gould, Ch. Munger, J. Alonso, P. Thieberger, and H. E. Wegner, *Phys. Rev. A* **32**, 3291 (1985) (paper III).
- ³R. Anholt, W. E. Meyerhof, H. Gould, Ch. Munger, J. Alonso, P. Thieberger, and H. E. Wegner, *Phys. Rev. A* **32**, 3302 (1985) (paper IV).
- ⁴R. Anholt and W. E. Meyerhof, *Phys. Rev. A* **33**, 1556 (1986) (paper V).
- ⁵R. Anholt, W. E. Meyerhof, X.-Y. Xu, H. Gould, B. Feinberg, R. J. McDonald, H. E. Wegner, and P. Thieberger, *Phys. Rev. A* **36**, 1586 (1987) (paper VIII).
- ⁶R. Anholt, H. H. Behncke, S. Hagmann, P. Armbruster, F. Folkmann, and P. H. Mokler, *Z. Phys. A* **289**, 349 (1979).
- ⁷E. Merzbacher and H. W. Lewis, in *Encyclopedia of Physics*, edited by S. Flügge (Springer, Berlin, 1958), Vol. 34, p. 166.
- ⁸G. S. Khandelwal, B. H. Choi, and E. Merzbacher, *At. Data* **1**, 102 (1969).
- ⁹G. Basbas, W. Brandt, and R. Laubert, *Phys. Rev. A* **17**, 1655 (1978).
- ¹⁰G. Basbas, W. Brandt, and R. Laubert, *Phys. Rev. A* **7**, 973 (1973).
- ¹¹J. Eichler, *Phys. Rev. A* **32**, 112 (1985).
- ¹²J. Eichler (private communication).
- ¹³J. Eichler, A. Tsuji, and T. Ishihara, *Phys. Rev. A* **23**, 2833 (1981).
- ¹⁴J. Eichler and F. T. Chan, *Phys. Rev. A* **20**, 104 (1979).
- ¹⁵F. T. Chan and J. Eichler, *Phys. Rev. A* **20**, 1841 (1979).
- ¹⁶J. Eichler, *Phys. Rev. A* **23**, 498 (1980).
- ¹⁷L. J. Dubé, in *Invited Papers of the Fourteenth International Conference on the Physics of Electronic and Atomic Collisions, Palo Alto, 1985*, edited by D. C. Lorents *et al.* (North-Holland, Amsterdam, 1986), p. 345.
- ¹⁸J. E. Golden and J. H. McGuire, *Phys. Rev. A* **12**, 82 (1975).
- ¹⁹J. H. McGuire, *Phys. Rev. A* **26**, 143 (1982).
- ²⁰V. Franco, *Phys. Rev. A* **22**, 937 (1980).
- ²¹J. H. McGuire, N. Stolterfoht, and P. R. Simony, *Phys. Rev. A* **24**, 97 (1981).
- ²²R. Anholt, *Phys. Lett.* **114A**, 126 (1986).
- ²³H. D. Betz, *Rev. Mod. Phys.* **44**, 465 (1972).
- ²⁴N. Bohr and J. Lindhard, *K. Dan. Vidensk. Selsk. Mat.-Fys. Medd.* **28**, No. 7 (1954).
- ²⁵H. D. Betz and L. Grodzins, *Phys. Rev. Lett.* **25**, 903 (1970).
- ²⁶The PPAC detector can be damaged by sparking, which in the isobutane gas can remove some of the aluminization on the Mylar. Since sparking is generally localized in the region where the beam strikes the detector, this can create holes in the electric field profile in certain spots. In this region, signals with reduced amplitudes or no signals are seen. This problem is particularly insidious since the outer window is unaffected; only the invisible inner window is affected. A bad detector was dissected to verify this behavior.
- ²⁷Rhombis Industries, Huntington Beach, California, part number TZB-12-5.
- ²⁸T. R. Dillingham, J. R. MacDonald, and P. Richard, *Phys. Rev. A* **24**, 1237 (1981).
- ²⁹J. H. Hubbel, W. Veigele, R. A. Briggs, R. T. Brown, D. T. Cromer, and R. J. Howerton, *J. Phys. Chem. Ref. Data* **4**, 471 (1975).
- ³⁰T. Kaneko, *Phys. Rev. A* **32**, 2175 (1985).
- ³¹J. M. Hansteen, O. M. Johnsen, and L. Kocbach, *At. Data Nucl. Data Tables* **15**, 3066 (1975).
- ³²R. L. Becker, A. L. Ford, and J. F. Reading, *J. Phys. B* **13**, 4059 (1980).
- ³³J. C. Slater, *Phys. Rev.* **36**, 57 (1930).
- ³⁴F. Bell and H. D. Betz, *J. Phys. B* **10**, 483 (1977).
- ³⁵H. C. Brinkman and H. A. Kramers, *Proc. Acad. Sci. Amsterdam* **33**, 973 (1930).
- ³⁶F. Biggs, L. B. Mendelsohn, and J. B. Mann, *At. Data Nucl. Data Tables* **16**, 202 (1975).
- ³⁷L. C. Northcliffe and R. F. Schilling, *Nucl. Data A7*, 233 (1970).
- ³⁸N. Bohr, *Phys. Rev.* **58**, 654 (1940).
- ³⁹W. E. Lamb, *Phys. Rev.* **58**, 696 (1940).
- ⁴⁰E. Baron, *IEEE Trans. Nucl. Sci. NS-19*, 256 (1972).

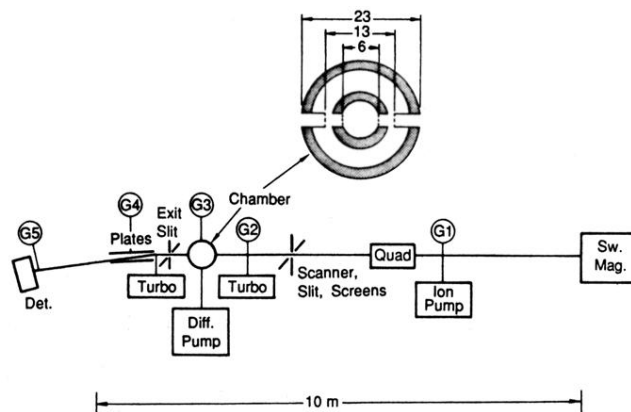


FIG. 1. Schematic diagram showing the layout of the experimental apparatus (to scale). Gauges G1, G2, G3, G4, and G5 are cold-cathode gauges. The 6-cm-diam inner-cell pressure is measured with a capacitance manometer. Quad, quadrupole magnet; Turbo, turbomolecular pump (260 l/sec); Diff. Pump, diffusion pump (1000 l/sec); Sw. Mag., switching magnet. The inner chamber dimensions are in centimeters.